Cell Insight 3 (2024) 100177

Contents lists available at ScienceDirect

Cell Insight

journal homepage: www.journals.elsevier.com/cell-insight

Letter to the editor

Structures of a sperm-specific sodium-hydrogen exchanger

Dear editor,

Capacitation is crucial for spermatozoa during fertilization in metazoans. To achieve capacitation, sperm flagellum must undergo a series of conserved signaling cascades directed by flagellum ion channels and transporters. The sperm-specific sodium-hydrogen exchanger, sNHE (also known as SLC9C1), plays a pivotal role in regulating hyperpolarization-induced intracellular alkalization. Notably, both *Slc9c1*-knockout mice (Wang et al., 2003) and individuals with *Slc9c1* mutations (Cavarocchi et al., 2021) exhibit reduced sperm motility, resulting in infertility. This condition is clinically known and diagnosed as asthenospermia.

sNHE/SLC9C1 belongs to the solute carrier 9 (SLC9) family of sodium-hydrogen exchangers (NHEs), widely believed to alkalize intracellular pH by utilizing the sodium gradient to extrude protons in an electroneutral manner. Mammalian NHEs are categorized into three subgroups (Pedersen & Counillon, 2019): 9A (NHE1-9), 9B (NHA1-2), and 9C (1–2). Strikingly, SLC9C1 is exceptional and distinguished by harboring a voltage-sensing domain (VSD) and a cyclic-nucleotide binding domain (CNBD), in addition to the NHE domain. Although VSD and CNBD typically function independently or in combination in voltage-gated ion channels (VGICs) and cyclic nucleotide (cNMP)-gated (CNG) channels, their functions and interplay have been confirmed in the sea urchin *Strongylocentrotus purpuratus* SLC9C1 (referred to as spSLC9C1 hereafter) (Windler et al., 2018). The VSD of spSLC9C1 was characterized as a genuine voltage sensor displaying a gating voltage of half-maximal activation ($V_{1/2}$) of −95 mV, while the binding of cAMP to CNBD shifts $V_{1/2}$ to −75 mV and prolongs the activity of ion transporting. This discovery thus underscores SLC9C1 as a unique ion transporter that is activated by hyperpolarization and modulated by cNMPs.

To understand the molecular underpinnings of spSLC9C1, we determined the cryo-electron microscopy (EM) structure of apo spSLC9C1 at 3.1 Å resolution, with C2 symmetry imposed (Supplementary Fig. S1 and Table S1). Most functional domains were visible except for VSD, of which the densities were weak and discontinuous. However, the local resolution of VSD was further improved to 3.5 to 4.0 Å by using focused 3D classification and local refinement. In our structures, apo spSLC9C1 forms a homodimer, with each protomer divisible into five distinct domains (Fig. 1b–d): a membrane-embedded NHE domain with 13 transmembrane helices (TM1-13); a VSD with helices S1-4; a coupling helices (CH) domain containing helices CH1-10; a peripheral CNBD facing inward; and a C-terminal domain (CTD) at the bottom.

The NHE of spSLC9C1 displays a typical NhaA fold (Hunte et al., 2005) and adopts an inward-facing conformation, resembling many other published eukaryotic SLC9 structures (Dong et al., 2021, 2022; Matsuoka et al., 2022) (Supplementary Fig. S2a). The structural similarity between the NHE of spSLC9C1 and that of other SLC9 members was estimated by the Cα root mean square deviation (r.m.s.d.) of superposition of NHE dimers. It turned out that the NHE of spSLC9C1 is more akin to that of the 9A subgroup (Cα r.m.s.d. around 2 to 3 Å), rather than that of 9B subgroup (Cα r.m.s.d. up to ~11 Å) (Supplementary Figs. S2b–e). While consistently, the inward-facing cavity in each NHE leaflet of spSLC9C1 is rich in negatively charged residues, including E149, D209, E231, D238, and E354, potentially mediating the entry and binding of sodium ions (Fig. 1e).

The VSD of spSLC9C1 was unambiguously modeled (Supplementary Fig. S3a) based on locally refined protomer map. It contains seven conserved Arg or Lys residues in a canonical $(R/K\text{-}XX)_n$ pattern on S4 (Supplementary Fig. S3c), and its folding pattern closely resembles that in other VGICs, despite some discrepancies (Supplementary Fig. S3d). Particularly, a short amphipathic horizontal membrane-anchoring S0 precedes S1, and S3 appears relatively straight. Most remarkably, the spSLC9C1 VSD forms an elongated S4 that protrudes from the membrane and seamlessly joins with CH7 in the cytoplasm. S4 and CH7 were measured to be ~35 and ~56 Å long, respectively, with an angle of 150° between them (refer to Supplementary Fig. S3e). The 'stem-like' structure of S4–CH7 indirectly links VSD to CNBD, which is situated ~77 Å away.

The CH of spSLC9C1 is sandwiched between NHE and CNBD-CTD, physically contacting all other four domains, namely NHE, VSD, CNBD, and CTD (Fig. 1f; Supplementary Figs. S4a–d). Intriguingly, model building discovered one extra intracellular α-helix in CH (CH3) and two additional β-strands at the extended end of CTD (β9 and β10) (Supplementary Fig. S4e), which were both unresolved in recently published spSLC9C1 structures (Chowdhury & Pal, 2023; Kalienkova et al., 2023; Yeo et al., 2023). Thus, we were allowed to observe various interactions between CH and the β9-10 from the other protomer (Fig. 1g). To avoid ambiguity, residues, structural elements, and domains in the other protomer were all marked with apostrophes herein. Specifically, β9′-10′ interacts with CH3-4 through extensive salt bridges and with CH1 via hydrophobic contacts. The loop connecting CH2 and CH3, containing a D541-D542-E543 negative residue triplet, though invisible, could potentially bring CH3 and β9′-10′ into close proximity by nonspecifically interacting with R479, R491, and R1209′ from TM13, CH1, and β9′-β10′ loop, respectively.

The CNBD of spSLC9C1 is positioned underneath CH helical bundles, with its cNMP-binding pocket facing towards the symmetry axis (Supplementary Figs. S5a–c). In contrast, the CNBDs in CNG channels and hyperpolarization-activated and CNG (HCN) channels have their cNMP-binding pockets facing outward. Despite this completely different orientation, the folding of CNBD in spSLC9C1 remains comparatively conserved (Supplementary Figs. S5d–h).

To elucidate the modulatory mechanism of CNBD, we set out to solve

https://doi.org/10.1016/j.cellin.2024.100177
Received 11 April 2024; Received in revised form 21 May 2024; Accepted 21 May 2024
Available online 30 May 2024

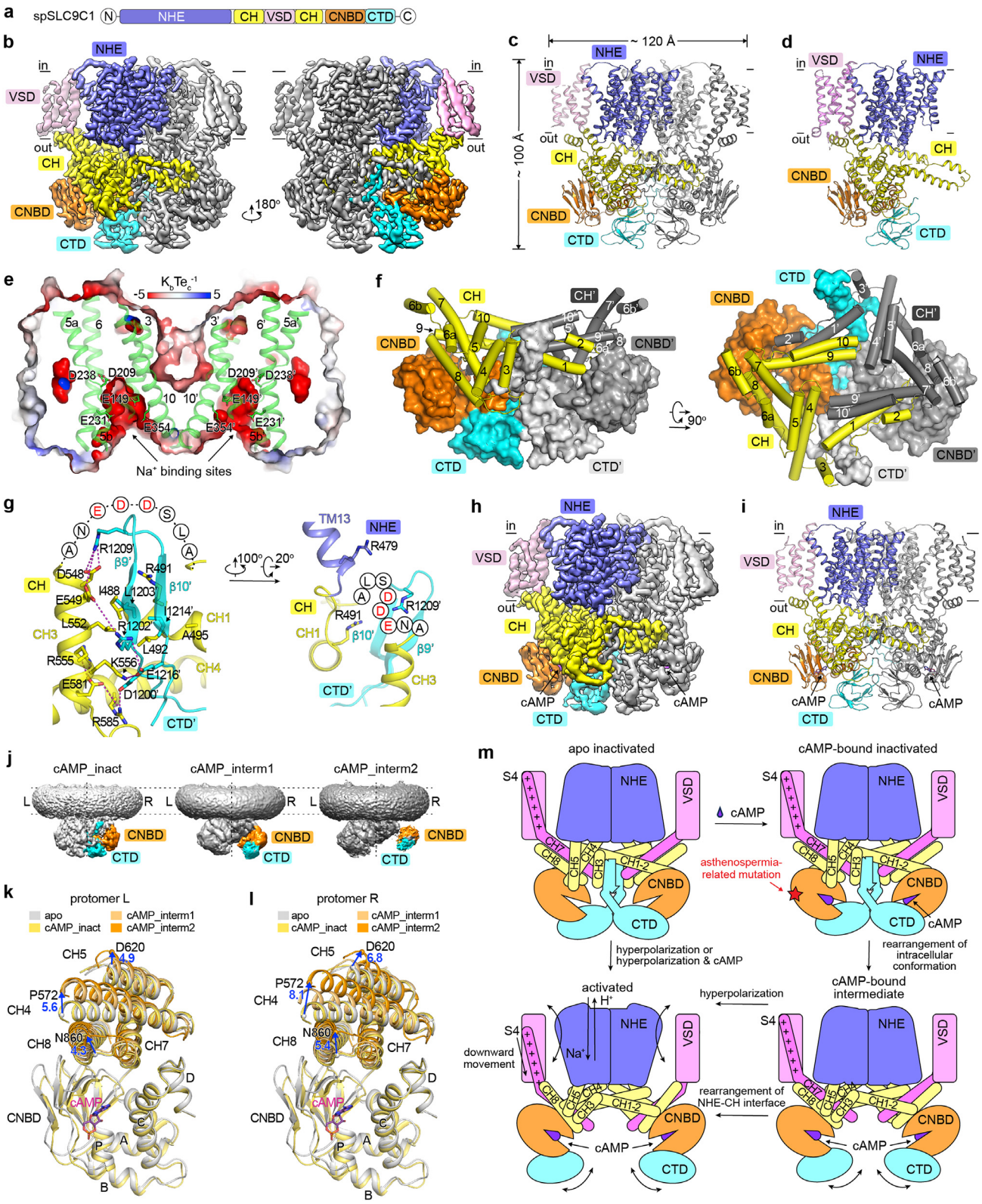

Fig. 1. Structures of spSLC9C1 in the apo and cAMP-bound states and cAMP-induced intracellular conformational changes. a, Domain architecture of full-length spSLC9C1. **b**,**c**, Cryo-EM map (**b**) and overall structure (**c**) of apo spSLC9C1. **d**, Structure of spSLC9C1 protomer in the apo state obtained from local refinement. **e**, Electrostatic potential surface (calculated with APBS plug-in in PyMol) of the NHE domain in apo spSLC9C1. The front half was cut away and the rear half was overlaid with TM3, TM5, TM6, and TM10. **f**, CH, CNBD and CTD in apo spSLC9C1. CH was shown as cartoon. CNBD and CTD were shown as surface. **g**, Interactions between NHE-CH and β9′-β10′ of CTD' in apo spSLC9C1. **h**,**i**, Cryo-EM map (**h**) and overall structure (**i**) of spSLC9C1 in the cAMP_inactivated state. **j**, Movements of CNBD and CTD upon binding of cAMP. The left (L) and right (R) protomers were separated by vertical dashed lines. **k**,**l**, Superposition of CH4-5, CH7-8, and CNBD from protomer L (**k**) and R (**l**) in the apo and different cAMP-bound states. **m**, Model for voltage-gated and cAMP-modulated activation of sodium-hydrogen exchange in spSLC9C1. Red star represents an asthenospermia-related exon skipping in-frame deletion mutation in the CNBD of human SLC9C1.

the structures of cAMP-bound spSLC9C1 in the presence of a saturating concentrating (2.5 mM) of cAMP. However, the dataset displayed large heterogeneity. After multiple rounds of focused 3D classification and refinement, we obtained three different structures, named cAMP_inactivated, cAMP_intermediate1, and cAMP_intermediate2 (Supplementary Figs. S6 and 7 and Table S2). Their resolutions are 3.15 Å (C2 symmetry), 3.77 Å (C1 symmetry), and 3.54 Å (C1 symmetry), respectively. Using the same strategy as above, the VSD of cAMP_inactivated was refined to a local resolution of 3.5–4.5 Å.

The structure of cAMP_inactivated is virtually identical to that of apo spSLC9C1, with a Cα r.m.s.d. of 0.537 Å (Fig, 1h, i and Supplementary Fig. S8c), indicating that cAMP_inactivated is indeed inactivated and has not undergone any of gating-related conformational rearrangements. Notably, cAMP was bound to both two protomers, as illustrated by the robust cAMP densities in the well-characterized binding pockets in CNBD (Supplementary Figs. S8e and f). Conversely, the structures of cAMP_intermediate1 and cAMP_intermediate2 reveal that binding of cAMP to CNBD causes conformational rearrangements in the intracellular domains, particularly in the CNBD and CTD (Fig. 1j), but not in the transport domain NHE, as shown by superposition of the apo and three cAMP-bound structures (Supplementary Fig. S9c). Those observations indicate that while binding of cAMP to CNBD is sufficient to induce rearrangement of intracellular conformation, but it is insufficient to trigger exchange of the inactivated state of spSLC9C1.

Ensemble and pairwise comparisons of the CH of apo and three cAMP-bound structures show that cAMP-binding to CNBD likely rearranges the intracellular part in an asymmetrical manner. Specifically, the CH helices in protomer R display larger movements than their counterparts in protomer L (Fig. 1k, l; Supplementary Figs. S9d–h). Among the ten helices in CH, CH4-5 and CH8, rather than others, undergo substantial displacements. They move upward towards the membrane plane predominantly at their VSD-distal ends, but to a lesser extent or not at all at their VSD-proximal ends. The movements for VSD-distal ends of CH4-5 and CH8 in protomer R were measured at 8.1, 6.8, and 5.4 Å at Cαs of P572, D620, and N860, respectively, compared with 5.6, 4.9, and 4.3 Å of their counterparts in protomer L. Interestingly, the movement is minimal in CH7, likely because CH7 is physically connected to S4 and locked by inactivation of VSD when the electrical force is absent. Moreover, densities for CH3 and β9′-10′ are completely gone in cAMP_intermediate1 and cAMP_intermediate2, suggesting those regions may function in intracellular stabilization in the apo and cAMP_inactivated states. Given the fact that the VSD of spSLC9C1 is gated by hyperpolarization, we expect S4 will undergo a vertical downward displacement after VSD activation. However, the binding of cAMP to CNBD appears to lower the energy barrier (shifting $V_{1/2}$ from −95 to −75 mV) for S4 movements by rearranging CH conformation, disrupting CH-CNBD and CH-CTD interaction, and destabilizing intracellular dimerization.

It should be noted that the rearrangement of intracellular conformation upon cAMP binding is continuous, and the observed cAMP_intermediate1 and cAMP_intermediate2 are only two of the many cAMP-bound inactivated intermediate states. The heterogeneity of the cAMP-bound dataset also confirms the existence of numerous other intermediate states, each displaying a variety of intracellular conformational changes. Furthermore, the asymmetrical nature of cAMP-induced conformational rearrangements suggests that the roles of two protomers, particularly their CH domains, may differ slightly in transporter activation.

The sperm-specific sodium-hydrogen exchanger SLC9C1 emerges as an extraordinary phylogenetic chimera, orchestrating a ligand-modulated gating mechanism to activate and regulate its ion-exchange activity. In our study, we observed interactions between CH3 and β9′-10′ in apo spSLC9C1, allowing specific explanation of dimerization and intracellular stabilization of this molecule; moreover, the three cAMP-bound structures reveal how cAMP-binding induces conformational rearrangements in the intracellular part, providing insights for understanding the mechanism of cAMP-modulated prolonged activation of spSLC9C1. Remarkably, a recent clinical study reported that an asthenospermia-related exon skipping mutation in human *Slc9c1* causes a 33 amino acids in-frame deletion (Δ 884–916 aa) in the CNBD domain (Supplementary Fig. S10) (Cavarocchi et al., 2021). We thus speculate that the resulting CNBD-damaged SLC9C1 may decouple the cAMP-modulated prolonged activation of this ion transporter, leading to defects and failures in hyperactivation and fertilization. In summary, we propose the model for cAMP-modulation of spSLC9C1 in the following scenarios: (1) when cAMP is unbound, the molecule is steadily inactivated (upper-left in Fig. 1m); (2) cAMP-binding alone is insufficient to activate the molecule (upper-right in Fig. 1m); (3) however, cAMP-binding is sufficient to induce intracellular conformational rearrangements to lower the energy barrier for VSD activation (lower-right in Fig. 1m); (4) hyperpolarization drives downward movement of S4 in VSD, removing its inhibition on CH7 and leading to transporter activation (lower-left in Fig. 1m).

Data availability

The authors declare that the data supporting the findings of this study are available within the paper. The cryo-EM density maps of apo and cAMP-bound spSLC9C1 have been deposited in the Electron Microscopy Data Bank (https://www.ebi.ac.uk/pdbe/emdb/) under accession numbers EMD-38559 (apo dimer), EMD-38565 (apo protomer), EMD-38568 (cAMP_inactivated dimer), EMD-38569 (cAMP_inactivated protomer), EMD-38570 (cAMP_intermediate1), and EMD-38571 (cAMP_intermediate2). The coordinates of the atomic models of apo and cAMP-bound spSLC9C1 have been deposited in the Protein Data Bank (http://www.rcsb.org) under accession numbers 8XPQ (apo dimer), 8XQ4 (apo protomer), 8XQ7 (cAMP_inactivated dimer), 8XQ8 (cAMP_inactivated protomer), 8XQ9 (cAMP_intermediate1), and 8XQA (cAMP_intermediate2).

CRediT authorship contribution statement

Hongyuan Qu: Validation, Methodology, Formal analysis, Data curation, Conceptualization. **Yi Zhen:** Methodology, Data curation. **Mohan Xu:** Methodology, Data curation. **Yan Huang:** Methodology, Data curation. **Yashu Wang:** Methodology, Data curation. **Gaoyuan Ji:** Methodology, Data curation. **Yuyu Zhang:** Validation, Supervision. **Haitao Li:** Validation, Supervision. **Zigang Dong:** Validation, Supervision. **Xiangdong Zheng:** Writing – review & editing, Writing – original draft, Visualization, Validation, Supervision, Resources, Project administration, Methodology, Investigation, Funding acquisition, Formal analysis, Data curation, Conceptualization.

Declaration of competing interest

The authors declare that they have no known competing financial interests or personal relationships that could have appeared to influence the work reported in this paper.

Acknowledgements

We thank Prof. Lei Chen from Peking University for gifting the vector of pBMCL1; Prof. Bailong Xiao from Tsinghua University and Prof. Jian Yang from Columbia University for insightful scientific disscussion; and Shuimu BioSciences for Cryo-EM facility access and technical support during image acquisition. This work was supported by the National Natural Science Foundation of China (32371292 to X.Z.).

Appendix A. Supplementary data

Supplementary data to this article can be found online at https://doi.org/10.1016/j.cellin.2024.100177.

References

Cavarocchi, E., Whitfield, M., Chargui, A., Stouvenel, L., Lores, P., Coutton, C., Arnoult, C., Santulli, P., Patrat, C., Thierry-Mieg, N., Ray, P. F., Dulioust, E., & Toure, A. (2021). The sodium/proton exchanger SLC9C1 (sNHE) is essential for human sperm motility and fertility. *Clinical Genetics, 99*, 684–693.

Chowdhury, S., & Pal, K. (2023). Architecture and rearrangements of a sperm-specific Na(+)/H(+) exchanger. *Res Sq [Preprint]*. rs.3.rs-3396005.

Dong, Y., Gao, Y., Ilie, A., Kim, D., Boucher, A., Li, B., Zhang, X. C., Orlowski, J., & Zhao, Y. (2021). Structure and mechanism of the human NHE1-CHP1 complex. *Nature Communications, 12*, 3474.

Dong, Y., Li, H., Ilie, A., Gao, Y., Boucher, A., Zhang, X. C., Orlowski, J., & Zhao, Y. (2022). Structural basis of autoinhibition of the human NHE3-CHP1 complex. *Science Advances, 8*, Article eabn3925.

Hunte, C., Screpanti, E., Venturi, M., Rimon, A., Padan, E., & Michel, H. (2005). Structure of a Na+/H+ antiporter and insights into mechanism of action and regulation by pH. *Nature, 435*, 1197–1202.

Kalienkova, V., Peter, M. F., Rheinberger, J., & Paulino, C. (2023). Structures of a sperm-specific solute carrier gated by voltage and cAMP. *Nature, 623*, 202–209.

Matsuoka, R., Fudim, R., Jung, S., Zhang, C., Bazzone, A., Chatzikyriakidou, Y., Robinson, C. V., Nomura, N., Iwata, S., Landreh, M., Orellana, L., Beckstein, O., & Drew, D. (2022). Structure, mechanism and lipid-mediated remodeling of the mammalian Na(+)/H(+) exchanger NHA2. *Nature Structural & Molecular Biology, 29*, 108–120.

Pedersen, S. F., & Counillon, L. (2019). The SLC9A-C mammalian Na(+)/H(+) exchanger family: Molecules, mechanisms, and physiology. *Physiological Reviews, 99*, 2015–2113.

Wang, D., King, S. M., Quill, T. A., Doolittle, L. K., & Garbers, D. L. (2003). A new sperm-specific Na+/H+ exchanger required for sperm motility and fertility. *Nature Cell Biology, 5*, 1117–1122.

Windler, F., Bonigk, W., Korschen, H. G., Grahn, E., Strunker, T., Seifert, R., & Kaupp, U. B. (2018). The solute carrier SLC9C1 is a Na(+)/H(+)-exchanger gated by an S4-type voltage-sensor and cyclic-nucleotide binding. *Nature Communications, 9*, 2809.

Yeo, H., Mehta, V., Gulati, A., & Drew, D. (2023). Structure and electromechanical coupling of a voltage-gated Na(+)/H(+) exchanger. *Nature, 623*, 193–201.

Hongyuan Qu
Academy of Medical Sciences, Tianjian Laboratory of Advanced Biomedical Sciences, State Key Laboratory of Esophageal Cancer Prevention and Treatment, Zhengzhou University, Zhengzhou, 450001, China
State Key Laboratory of Molecular Oncology, MOE Key Laboratory of Protein Sciences, SXMU-Tsinghua Collaborative Innovation Center for Frontier Medicine, School of Medicine, Tsinghua University, Beijing, 100084, China
Beijing Frontier Research Center for Biological Structure and Beijing Advanced Innovation Center for Structural Biology, Beijing, 100084, China

Yi Zhen, Mohan Xu
Academy of Medical Sciences, Tianjian Laboratory of Advanced Biomedical Sciences, State Key Laboratory of Esophageal Cancer Prevention and Treatment, Zhengzhou University, Zhengzhou, 450001, China

Yan Huang
Academy of Medical Sciences, Tianjian Laboratory of Advanced Biomedical Sciences, State Key Laboratory of Esophageal Cancer Prevention and Treatment, Zhengzhou University, Zhengzhou, 450001, China
Key Laboratory of Geriatric Nutrition and Health, Beijing Technology and Business University, Beijing, 100048, China

Yashu Wang
Academy of Medical Sciences, Tianjian Laboratory of Advanced Biomedical Sciences, State Key Laboratory of Esophageal Cancer Prevention and Treatment, Zhengzhou University, Zhengzhou, 450001, China

Gaoyuan Ji
State Key Laboratory of Molecular Oncology, MOE Key Laboratory of Protein Sciences, SXMU-Tsinghua Collaborative Innovation Center for Frontier Medicine, School of Medicine, Tsinghua University, Beijing, 100084, China
Beijing Frontier Research Center for Biological Structure and Beijing Advanced Innovation Center for Structural Biology, Beijing, 100084, China

Yuyu Zhang
Key Laboratory of Geriatric Nutrition and Health, Beijing Technology and Business University, Beijing, 100048, China

Haitao Li
State Key Laboratory of Molecular Oncology, MOE Key Laboratory of Protein Sciences, SXMU-Tsinghua Collaborative Innovation Center for Frontier Medicine, School of Medicine, Tsinghua University, Beijing, 100084, China
Beijing Frontier Research Center for Biological Structure and Beijing Advanced Innovation Center for Structural Biology, Beijing, 100084, China

Zigang Dong[*], Xiangdong Zheng[**]
Academy of Medical Sciences, Tianjian Laboratory of Advanced Biomedical Sciences, State Key Laboratory of Esophageal Cancer Prevention and Treatment, Zhengzhou University, Zhengzhou, 450001, China

[*] Corresponding author.

[**] Corresponding author.
E-mail addresses: dongzg@zzu.edu.cn (Z. Dong), zhengxd@zzu.edu.cn (X. Zheng).